06

# Minimization of thermal distortions arising in optical elements under the influence of intense X-ray sources (Review)

© V.V. Lider

Shubnikov Institute of Crystallography „Crystallography and Photonics“ Russian Academy of Sciences,
119993 Moscow, Russia
e-mail: vallider@yandex.ru

*Received July 16, 2023*
*Revised October 9, 2023*
*Accepted October 18, 2023*

The paper considers various methods for compensating thermal stresses caused by intense beams of X-ray synchrotron radiation and free electron laser radiation. Methods for cooling silicon monochromators and mirrors using liquids such as water, liquid gallium and liquid nitrogen are described. Particular attention is paid to the description of the possibilities of using synthetic diamond crystals as cooled monochromators.

**Keywords:** synchrotron radiation, free electron laser, thermal loads, X-ray monochromators, X-ray mirrors, cooling liquids.

DOI: 10.61011/JTF.2024.01.56897.179-23

## Introduction

Sources of synchrotron radiation (SR) and X-ray free electron lasers (FEL) are unique instruments that ensure extremely bright X-ray radiation allowing for visualization of the matter with atomic spatial resolution [1]. Synchrotron light sources consist of circular electron accelerators with SR output from rotary magnets and undulators. X-ray FEL systems are based on linear electron accelerators and generate more coherent and shorter pulses suitable for time-resolved experiments.

The current strength and pulse duration is the main difference between the two types of systems: while synchrotrons have peak currents per electron bunch of the order of 10 A and pulse duration of tens of picoseconds, X-ray FEL systems generate kA peak currents with pulse duration at the femtosecond level.

FEL generate radiation with significantly higher power levels and a lower energy bandwidth than SR systems: while X-ray FEL can generate pulse energy at the mJ level with a relative bandwidth of $10^{-4}$, synchrotrons generate nJ pulse energy and a much larger relative bandwidth. In general, the peak brightness of the radiation produced by X-ray FEL is much higher than peak brightness of radiation of synchrotron systems. For example, the beam of the new source „Sirius“ at the Brazilian Synchrotron Light Laboratory (LNLS) reaches the first crystalline monochromator with a power of less than 7 W and a size of $1.5 \times 2.6$ mm. The power density is less than 2.5 W/mm$^2$ at an almost normal drop [2]. At the same time, the FEL of the Linac Coherent Light Source (LCLS) of the SLAC National Accelerator Laboratory has a pulse energy of about 2 mJ, a transverse spot size of about 150 $\mu$m and a pulse duration of about 100 fs. The calculation of the average absorbed heat flux during the pulse provides the value $4 \cdot 10^{13}$ W/m$^2$ [3].

Nevertheless, synchrotrons have their advantages: firstly, they provide a much higher repetition rate than X-ray FEL, which is beneficial for many experiments. The differences of the average brightness become much less pronounced than the difference of the peak brightness values taking into account the higher repetition rates and longer pulses at synchrotrons. Another advantage of synchrotrons is related to accessibility for users. It is much easier to access synchrotrons than X-ray FEL since the number of synchrotrons (more than 50 worldwide) is much greater than the number of X-ray FEL systems (from 5 to 10), and since each synchrotron has more channels (up to about 50) than X-ray FEL (up to about 10).

It is possible to say that both synchrotrons and X-ray FEL are invaluable research tools capable of visualizing matter with a spatial resolution at the atomic level [4].

However, the thermomechanical deformation of optical elements caused by a large thermal load is one of the obstacles to delivering a large flow of SR photons to the experimental station with minimal loss. The purpose of the review is to describe methods for compensating thermal deformations.

## 1. Thermal loads

Often, the first optical element subjected to a powerful thermal load is a monocrystalline monochromator.

Three different types of distortions occur in the crystal due to high thermal loads. Firstly, there is a general curvature of the crystal caused by the thermal expansion of the upper part of the crystal in a direction parallel to the surface. Secondly, a thermal bump is formed caused by the thermal expansion of the crystal in a direction perpendicular to the surface. The third type of distortion is a change in the distance between the planes of the crystal at its surface

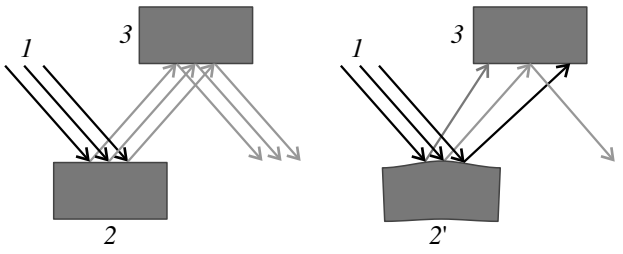


**Figure 1.** Illustration of the effect of thermal distortions on the intensity of a doubly diffracted beam (*1* — polychromatic SR beam, *2* — ideal first monochromator crystal, *2'* — the first monochromator crystal with thermal „hump", *3* — the second crystal is a monochromator) [6].

due to thermal expansion. This results in a change of the energy of diffracted photons [5].

The first crystal selects the desired X-ray energy in a typical two-crystal monochromator at the SR station, and the second crystal redirects the formed beam in the direction of the experimental station (Fig. 1). In this case, the first crystal absorbs most of the incident power of polychromatic radiation.

The strongly collimated incident X-ray beam will diverge after reflection as a result of thermal distortions created by temperature gradients in the first monochromator crystal, so that photons of different energies will have different directions, and the second crystal will no longer be able to simultaneously reflect all X-rays diffracted on the first crystal (Fig. 1).

Consequently, the throughput of a two-crystal monochromator will be reduced by one or two orders of magnitude [7]. Therefore, the task is to find an engineering way to a solution capable of minimizing intensity losses caused by thermal deformations of the monochromator. However, first of all, it is necessary to be able to measure these deformations.

## 2. Metrology

The change of the shape of the crystal surface because of the thermal deformations and distortion of the crystal volume (thermal stress) can significantly change the diffraction properties of the crystal in the case of high thermal load and, consequently, result in a broadening of the X-ray rocking curve. Therefore, most of all studies of crystals under high thermal load were carried out by modeling the deformation field in a thermally distorted crystal using the finite element method (FEM) and comparing its results with the rocking curve of a double monochromator crystal, which is a convolution of the rocking curves of the first distorted crystal and the second perfect crystal [8–11]. This convolution gives an integral over the area of the beam footprint with the loss of all details of the complex distribution of thermal distortions.

The measurement of the surface shape of a distorted crystal *in situ* under high thermal load is significantly simplifies the solution of the problem.

There are several approaches to visualizing distorted surfaces. The flatness of the reflecting surface can be estimated up to microradian over a large area using optical methods such as long-trace profiling (LTP) [12]. This method provides excellent accuracy in determining the shape of the surface, but it provides information only along the line. Therefore, obtaining information about the wavefront formed by X-ray diffraction on a crystal subjected to thermal shock is a more effective way to determine thermal deformations.

The wavefront sensor is one of the most effective elements of the metrology system. Its task is to measure the curvature of the wavefront and transmit these measurements to the processing device. There is a wide variety of wavefront sensors [13]. They include Shack-Hartmann sensors [14], as well as sensors based on the Talbot effect [15], X-ray speckles [16] and ptichography [17]. For example, the effect of heat stroke on the characteristics of a two-crystal silicon monochromator was studied in [18] using a two-dimensional Talbot interferometer.

The wavefront sensors listed above, as a rule, provide wavefront measurement only periodically and usually invasively, interrupting the experiment and wasting valuable time. Non-invasive measurements can be performed in various ways. For example, the authors of [19] proposed a method for mapping the three-dimensional distortion of a crystal under the impact of heat shock. The method is similar to the Shack-Hartmann method and is based on the idea that a distorted reflective surface corresponds to its distorted image. The metal mask *2* (Fig. 2) has a series of evenly spaced holes that create an array of light points using a flat light source located behind the mask. The light from the array of dots is reflected from the crystal surface and recorded by a CCD camera *3*. The holes in the mask in the experiment had a diameter of 0.3 mm and were spaced at a distance of 1.5 mm from each other on an area of $100 \times 100$ mm. Image frames *4* were analyzed using the Centroid [20] program. This program calculates the position of the center of gravity of each light point in the image.

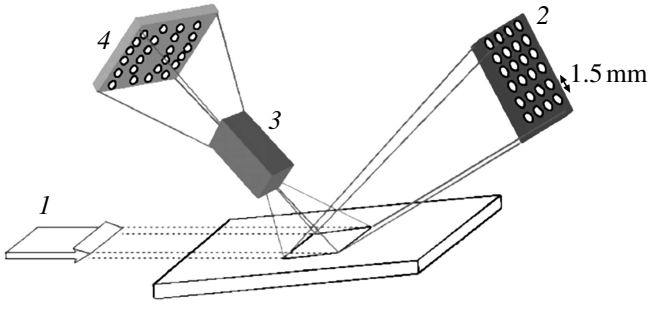


**Figure 2.** Schematic diagram of heat shock measurement: *1* — X-ray beam, *2* — metal mask, *3* — CCD camera, *4* — mask image [19].

## 3. Methods for compensation of thermal stresses on SR sources

As mentioned above, the effect of an intense SR beam on an X-ray optical element can lead to the appearance of a thermal „hump" on its surface. Its curvature $\varkappa$ at the vertex does not depend on the thickness of the irradiated element and is given by the expression

$$\varkappa \approx \alpha Q/k, \tag{1}$$

where $\alpha$ — coefficient of thermal expansion ($K^{-1}$), $k$ — thermal conductivity [$W \cdot cm^{-1} \cdot K^{-1}$] of the X-ray optical element, $Q$ — the energy density of the SR beam absorbed by the element [$W \cdot cm^{-2}$]. In this case, the slope angle of the reflecting planes $\Delta\theta_{aver}$ averaged over the „hump" (usually called the slope error) will be

$$\Delta\theta_{aver} \approx \varkappa \Delta L, \tag{2}$$

where $\Delta L$ — the length of the thermal „hump" in the diffraction plane.

Subbotin et al. [21] showed for a simple model (a crystal block heated from above and cooled from below) in which all power is absorbed on the surface that the error of the slope of the surface $\Delta\theta$ is given by the formula:

$$\Delta\theta_{aver} = F(\alpha/k)(T)Q, \tag{3}$$

where $F$ is a constant depending on the diffraction geometry, the size of the beam trace and the cooling method [22].

The reduction of the slope error can be achieved in several ways according to the formula (3):

1) selecting the material of the X-ray optical element with the minimum ratio value $\alpha/k$;

2) selecting the optimal cooling mode for the X-ray optical element;

3) reducing the density of the absorbed power of the SR beam by an X-ray optical element.

### 3.1. Selection of materials

It was proposed in 1986 to use the special thermal properties of diamond-like semiconductors, such as silicon and germanium, in which the coefficient of thermal expansion at low temperatures passes through zero (Fig. 3), and thermal conductivity increases significantly at cryogenic temperatures (Table. 1) [23,24]. Both of these changes in properties are favorable for optics at high thermal loads and represent a real gift from nature to the naturalist [7].

Silicon and germanium are successfully used in X-ray optics. Silicon single crystals are attractive because they have an almost perfect crystal lattice and are commercially available in large quantities [25].

However, many applications (for example, monochromatization of FEL radiation with very high average and peak power) require greater efficiency than silicon can provide: transparency for X-rays, resistance to radiation damage, mechanical strength, high X-ray reflection coefficient in Bragg

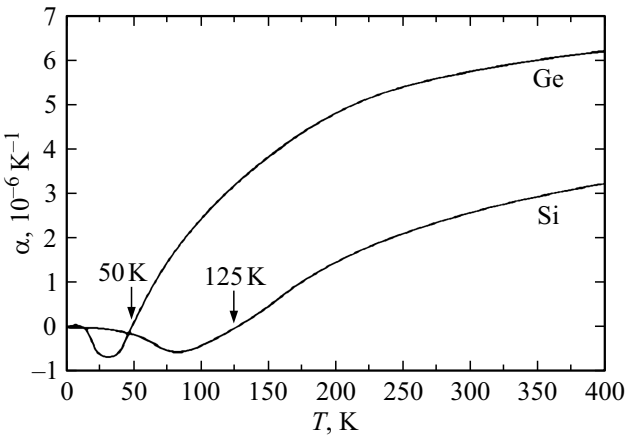


**Figure 3.** Coefficient of thermal expansion of silicon and germanium. The coefficient of thermal expansion of silicon is zero at 125 K[7].

**Table 1.** Properties of diamond IIa, Si and Ge, important for X-ray applications [25]

| Material | Diamond IIa | Si | Ge |
|---|---|---|---|
| Atomic number Z | 6 | 14 | 32 |
| Absorption coefficient, $\mu$, ($E = 8$ keV) ($cm^{-1}$) | 14 | 143 | 350 |
| Thermal conductivity, $\kappa$, at 297 K ($W \cdot cm^{-1} \cdot K^{-1}$) | 20−25 | 1.5 | 0.64 |
| Thermal conductivity, $\kappa$, at low temperature ($W \cdot cm^{-1} \cdot K^{-1}$) | 150 (80 K) | 3.25 (80 K) | 2.32 (100 K) |
| Coefficient of thermal expansion, $\alpha$ 297 K ($W \cdot cm^{-1} \cdot K^{-1}$) | 1 | 2.4 | 5.6 |
| Quality indicator, $100 \times \kappa/\mu\alpha$ at 297 K (MW) | 36−250 | 0.44 | 0.03 |

geometry and thermal conductivity. In such cases, diamond is the preferred material, since it surpasses silicon with its unsurpassed radiation resistance, orders of magnitude higher thermal conductivity [26], low coefficient of thermal expansion [27] and almost 100% reflectivity in the field of Bragg diffraction [28] (Table 1).

Both high modulus of elasticity and fracture strength are additional favorable properties of diamond. The average value of the elastic modulus of diamond is 1035 GPa compared with the average elastic modulus of silicon of 191 GPa. The Young modulus of diamond is fairly constant with an anisotropy coefficient of 1.21 in all directions (the anisotropy coefficient of silicon is 1.44). This unique combination of outstanding properties makes diamond the most promising material for transparent, elastic components

of high-resolution X-ray optics that preserve the wavefront, which is necessary for a bright and highly coherent next-generation light source such as FEL [29].

The absorbed X-ray power ($P_a$) is defined as follows for the symmetric Bragg case: $P_a = P_o \exp(-\mu t/\sin\theta_B)$, where $P_o$ — incident crystal power, $\mu$ —linear absorption coefficient, $t$ — crystal thickness, $\theta_B$ — Bragg angle. Therefore, the quality indicator characterizing the immunity of the crystal to thermal loads can be defined as $\kappa/(\alpha\mu)$, which is listed in Table 1 for various materials. This quality indicator at room temperature, for diamond is two orders of magnitude higher than quality indicator of silicon.

Most single crystals of natural diamond belong to type Ia with a nitrogen concentration of several tens to several hundred parts per million, while single-crystal diamond of type IIa has a small amount of nitrogen (less than ten parts per million). A single crystal diamond of type IIa is extremely rare in nature; it probably accounts for less than 2% of existing natural diamonds [30]. Currently, synthetic materials are structurally superior to the best natural materials by several orders of magnitude [31].

In recent years, single crystal diamond has not been the preferred material for X-ray optical elements because of its low perfection and small size. The size of an optical element (for example, a monochromator) can determine the cross-sectional area of the X-ray beam produced by it and, therefore, limit the size of the studied object. Therefore, despite the attractive properties of diamond, silicon is mainly used for the production of most X-ray optical elements.

### 3.2. Selection of coolants

The most common way to prevent thermal stresses in optical elements such as monochromators and mirrors is to cool them with liquids. The cooling mechanisms are based on the convective heat exchange of the liquid flow with the surface of the X-ray optical element.

The water cooling is currently the most common method of removing heat from X-ray optical components. The use of liquid metals as a refrigerant for X-ray optics components is an alternative approach. Liquid metals ensures a significant improvement of the cooling efficiency compared to water because of their thermal and physical properties. Liquid metals, as a rule, have high thermal conductivity, high volumetric heat capacity and a wide range of operating temperatures. Bismuth, tin, lithium and indium are excellent coolants, especially lithium, with its very high thermal conductivity and very high specific heat capacity per unit volume. However, these four substances were rejected due to their moderately high melting points. The next two, sodium and potassium, are also very good coolants. Their operating temperature ranges are smaller than operating temperature ranges of the previous candidates, but still quite high, and they would be the first candidates for the role of preferred coolant if there was no better option. Their main disadvantage is that they strongly interact with oxygen and water and, for this reason, pose a possible fire hazard and require special handling procedures. Liquid rubidium has all the necessary characteristics to create an excellent coolant, and it could be considered if it were not so expensive. Gallium and caesium have quite acceptable melting points, just above room temperature, and good thermal conductivity. Gallium was chosen instead of caesium because of its much higher specific heat capacity per unit volume, better operating temperature range, much lower vapor pressure, and its much less reactive nature in case of exposure to oxygen and water. Low steam pressure is very important for operation in a high vacuum environment. Mercury was rejected because of its poor thermal conductivity, low operating temperature range and very high vapor pressure. Leakage in the mercury cooling circuit will be serious even at room temperature and very serious at elevated temperatures.

Liquid gallium is most promising liquid metal coolant identified to date, which appears to have all the desired properties and the least number of undesirable properties of the liquid metals studied. A very low vapor pressure over a broad range of operating temperatures makes liquid gallium an ideal coolant for use in high vacuum conditions in addition to the special properties of liquid metals that make them good heat carriers [32].

Liquid gallium has relatively good physical properties compared to water, which makes it attractive for use as a coolant. Moreover, gallium becomes liquid at 29.8°C, and its melting point decreases to 16°C when it is fused with indium to its eutectic form (76 mass.% Ga−24 mass.% In) and it becomes liquid at room temperature. Further fusion of gallium with Sn and Zn (61 mass.% Ga, 25 mass.% In, 13 mass.% Sn and 1 mass.% Zn) reduces the melting point to 10°C [33].

The main differences for different coolants in the calculations of diffraction crystal distortions are related to different values of the heat transfer coefficient $h$. The amount of heat that is transferred by the coolant per unit area of a solid per degree of temperature is described by this parameter that depends on the cooling model describes [7]:

$$h = A_1 k/d + A_2(k^{0.6}C_v^{0.4}/d^{0.2}v^{0.8})V^{0.8}, \qquad (4)$$

where $k$ — thermal conductivity of the coolant, $C_v$ — volumetric heat capacity, $V$ — coolant velocity, $v$ — kinematic viscosity, $d$ — a distance similar to the hydraulic diameter of the cooling channel, $A_1$, and $A_2$ — coefficients allowing empirical consideration of the geometry of the cooling channels.

The first term is a constant depending on the thermal conductivity of the liquid and the shape of the cooling channels. The second term is a function of many variables and has an almost linear dependence on the velocity of the liquid. The very low thermal conductivity of water compared to gallium makes $h$ very small for water at low flow rates; thus, water is a poor coolant at low flow rates. The second term dominates at high flow rates, but even

**Table 2.** Comparison of heat transfer properties of liquid gallium, water, liquid nitrogen and liquid propane

| Substance | $k$ [W/(cm·K)] | $C_v$ [J/cm$^3$] | $k^{0.6}Cv^{0.4}/v^{0.8}$ |
|---|---|---|---|
| Ga(50°C) | 0.33 | 2.22 | 90.0 |
| $H_2O$(20°C) | 0.006 | 4.19 | 5.34 |
| $N_2$(−170°C) | 0.0014 | 1.60 | 4.57 |
| $C_3H_8$(−170°C) | 0.0020 | 1.40 | 1.38 |

Note. $k$ —thermal conductivity of the coolant, $C_v$ — volumetric specific heat [5].

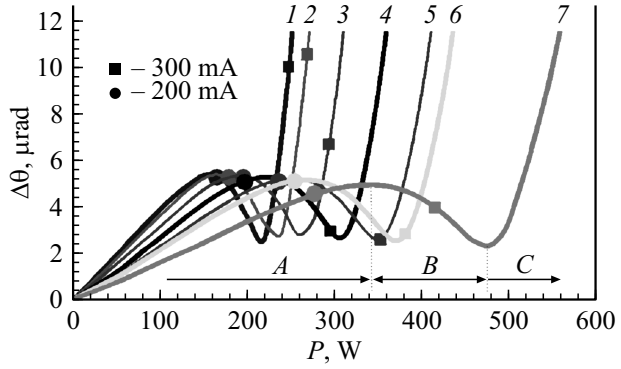


**Figure 4.** RMS error of the temperature slope $\theta$ of a silicon crystal cooled with liquid nitrogen under variable thermal load $P$ at different Bragg angles $\theta_B$ (*1* — 23.1 °, *2* — 20.1 °, *3* — 16.0 °, *4* — 12.3 °, *5* — 10.2 °, *6* — 9.4 °, *7* — 6.6 °). *A* — linear region, *B* — transition region, *C* — nonlinear region (see explanations in the text) [10].

here $h$ continues to be noticeably higher for gallium than for water.

Table 2 lists important thermal properties for gallium, water, liquid nitrogen and liquid propane. Gallium is by far the most efficient coolant in this group. Liquid nitrogen and liquid propane are cooling liquids at sufficiently low temperatures and they can be used to cool silicon down to 125 K. The coefficient of thermal expansion of silicon passes through zero at this temperature, and the thermal conductivity increases fourfold. The silicon crystal is very resistant to thermal distortion at temperatures of about 125 K and can remove a large amount of heat from its surface with small thermal gradients. Fig. 3 illustrates these features for both silicon and germanium crystals. The main difference between liquid nitrogen and liquid propane as refrigerants is their useful operating temperature range. The range of 14 K (63−77 K) of liquid nitrogen at 1 atm is significantly less than the operating range of 145 K (86−231 K) of propane. This difference is very important if large thermal loads need to be removed.

The efficiency limits of a cryogenically cooled silicon monochromator have been studied theoretically using FEM [10,30,34]. The dependence of the RMS error of the thermal slope of a silicon crystal on the absorbed power at various Bragg angles was plotted (Fig. 4) for the experimental beamline UPBL6 of the European Synchrotron Radiation Facility (ESRF) [10]. It is easy to determine where the working points of a silicon crystal are located at an electron beam current of 200 and 300 mA.

Three areas of radiation power can be defined [10,30,35]:

1) linear area: the temperature slope error is linearly proportional to the power consumption in this area. The crystal temperature is less than 125 K.

2) transition area: the temperature of the Si crystal, at which the coefficient of thermal expansion is zero, is about 125 K. In this case, the thermal slope error is minimal.

3) Nonlinear area: the thermal slope error increases rapidly with power, and the crystal temperature is more than 125 K [30].

The results obtained are convenient for the development and optimization of a monochromator on a silicon crystal. The idea is not to operate in the non-linear area.

The surface of the cryogenically cooled silicon crystal is concave at low thermal load (which corresponds to the negative values of the parameter $\alpha$ in Fig. 4), it is convex at high thermal load and has a complex shape, almost flat in average under the medium thermal load [11]. The detailed shape of a thermally deformed silicon crystal significantly affects the wavefront of the beam at the output of the monochromator. A parallel X-ray beam can become convergent (divergent) when the crystal is thermally deformed into a concave (convex) shape [10].

There are two ways of interaction of the coolant with the X-ray optical element such as direct and indirect. The liquid directly cools the element in case of direct (internal) cooling; the heat generated in the element is removed by cooling units in contact with it in case of indirect (contact) cooling.

### 3.3. Direct cooling methods for crystal monochromators

The three most common direct cooling geometries are shown in Fig. 5. Cooling of the lower surface of a flat plate (geometry of a flat plate) (Fig. 5, *a*) is the simplest and most common approach used when thermal loads are only a few W/cm$^2$. For example, the first crystal of a two-crystal monochromator was subjected to direct cooling in [36,37] (Fig. 6). It consists of a thin-walled silicon „box“, the bottom of which is glued to a stainless steel water collector; water is supplied through jet tubes directed perpendicular to the back of the crystal.

The cooling channels located directly under the working surface of the monochromator (Fig. 5, *b*, *c*) are much more efficient. Such channels should obviously be located as close as possible to the heated surface. A thin (and therefore flexible) layer of material known as a hot wall is above the channels. It has a temperature gradient across it which, if not compensated, will result in a convex curvature of the layer. There is a large thick block under the channels, which

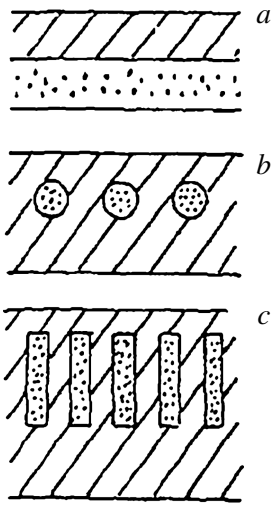


**Figure 5.** Diagrams of three common direct cooling geometries [5] (see explanations in text).

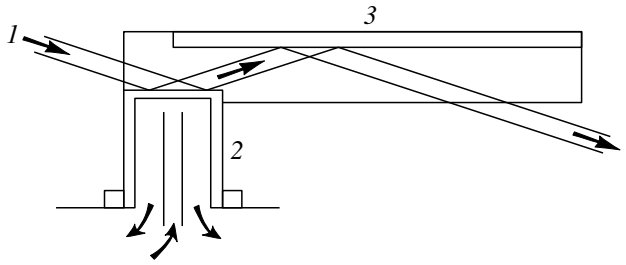


**Figure 6.** The scheme of direct cooling of the first arm of a two-crystal monoblock monochromator (*1* — a beam of SR; *2*, *3* — the first and second arms of the monochromator, respectively; the arrows show the direction of water circulation) [37].

should have significantly greater rigidity (thickness) than the hot wall [38].

It may seem that the use of circular cooling channels reduces the liquid-crystal surface for heat removal, but such a geometry actually increases the effective heat transfer by 57% and reduces $\Delta T$ between liquid and crystal by a similar amount compared to the geometry of a flat plate. Channels with a rectangular profile can further increase the heat exchange area: „the cooling effect of the ribs“ allows much more heat to be removed for a fixed $\Delta T$ than in the case of a flat geometry. The shape of the channels shown in Fig. 5, *c* increases the heat transfer coefficient by 5 times. This approach will help to reduce the amount of the heat shock by reducing the average temperature in the upper part of the crystal [7].

The creation of a direct water-cooled monochromator with 11 small holes (diameter 1.5 mm) drilled along the width of the crystal near its optical surface was reported in [39].

The channel sizes tend to decrease (formula (4)) for optimal heat transfer, and the manufacture of channels by drilling becomes difficult. Therefore, a silicon monochromator usually consists of two halves: a front panel with cooling channels and a lower support volume (Fig. 7, *a*). The mating blocks are polished after any mechanical treatment to provide flat surfaces for the subsequent bonding procedure. The use of water-cooled microchannels (MC) in silicon X-ray monochromators with dimensions optimized for effective compensation of thermal stresses was investigated in [40]. Such channels usually have a width of about $40\,\mu$m and a depth of $400\,\mu$m. The MC can be cut with a diamond saw, and the support volume is machined with diamond end mills and core drills [41]. The two halves are connected after machining. The compound should have the following properties for direct-cooled monochromator applications: minimal deformation caused in the crystal, radiation resistance for a long service life, and tightness to prevent coolant leaks into the vacuum system [42].

Several methods of coupling have been reported in the literature [43,44]. The common feature of all methods is that they deform the crystal lattice [45]. Significant deformations can be introduced into the crystal during its manufacture and connection.

The authors of [46] proposed three new MC designs and compared them with the „classical“ MC layout. The designs are shown schematically in Fig. 7. The overall design strategy is to reduce the deformation created by joining two silicon blocks. All three MC models show a smaller increase of the width of the rocking curve.

The design of MC„2+1“ was tested for reducing the deformation area (Fig. 7, *b*). The idea of design 2+1 is to eliminate contacts between two ribs out of every three and increase the third fin. The reduction of the contact area between the two volumes reduced the deformation surface. The increase of the space for the coolant flow between the ribs is one of the advantages of this approach because it reduces the need for high liquid pressure (high pressure due

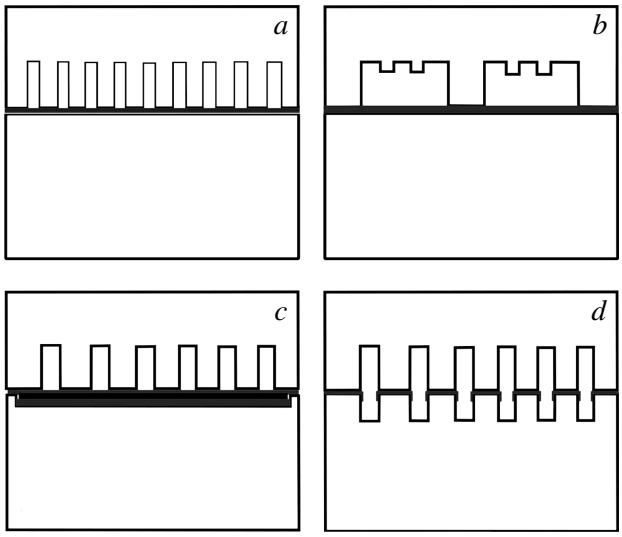


**Figure 7.** Proposed geometry of microchannels: *a* — classical design, *b* — 2+1 design, *c* — „sandwich“ design, *d* — „rib-to-rib“ design [46].

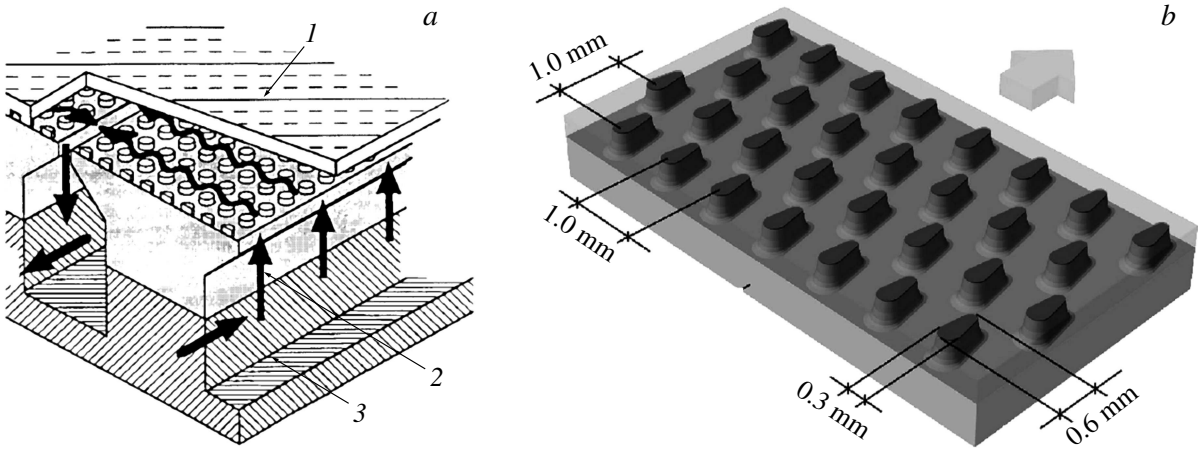


**Figure 8.** *a* — diagram of the pin cooling model (*1* — upper plate of a silicon monochromator with pins, *2* — lower support volume, *3* — metal holder). The arrows show the directions of the water flow [52]. *b* — an example of the design of the upper plate of a monochromator (the arrow indicates the direction of the water flow) [53].

to the flow of the cooling medium can deform the crystal surface). In addition, two small ribs between the wider ribs reinforce the monochromator structure.

The second proposed design consists of a classic upper and lower support volumes. 0.5 mm thick silicon transition insert was placed between the upper and lower support volumes to reduce the deformation. The function of this middle part is to compensate and absorb voltage. The third MC design employed the „rib-to-rib“ concept (Fig. 7, d). The advantage of the „rib-to-rib“ design is the small contact area between the upper and lower volumes of silicon and the absence of lateral deformation.

From the experimental rocking curves and models constructed by the FEM method, it follows that the proposed MC designs represent a significant improvement. The classic MC design had an average increase of the rocking curve by about 8 mrad in case of use of aluminum solder and a layer of silicon with a thickness of 1 mm above the MC. The „rib-to-rib“ design reduces this value to 5 mrad, and by increasing the layer above the MC to 2 mm, it can be reduced to less than 2.5 mrad. However, this increases the temperature of the working surface because of the lower cooling efficiency by several degrees [46], while smoothing out temperature fluctuations.

Water [40,43,46,47] or liquid gallium [33,48,49] is used as coolants for controlling thermal stresses of monochromators with MC; cryogenic cooling is used relatively rarely [50,51].

Pin heat exchangers should also be considered when water is used as a coolant [42,52,53]. Figure 8 shows a pin cooling model. The cooling zone is divided into several cells, including a set of pins. The pins in the cell interrupt the flow of water and then create a turbulent flow to obtain a greater heat transfer coefficient.

When dividing a large cooling area into small cells of suitable size, not only a small pressure drop is maintained due to short water flow paths, but the entire area is cooled evenly. The effect is that at real pressures, the coolant flow velocity near the hot wall is an order of magnitude higher than the velocity that can usually be obtained in channels with a uniform cross section [38]. The heat transfer coefficient of the pin cell system is 2–4 times greater than the heat transfer coefficient of the MC system with the same liquid velocity (as follows from the formula (4), the higher the speed, the greater the heat transfer coefficient).

The process of manufacturing a crystal with a cellular pin structure consists of two stages. A honeycomb structure of pins is fabricated at the first stage, and silicon wafers are coupled at the other stage. The authors of [52] produced arrays of pins using sandblasting. This is simple and inexpensive method for creating shallow channels. The average diameter of the pins is about 0.3 mm, the height of the pins is about 0.2 mm, the pitch of the pins is about 0.5 mm. Au/Si eutectic was used to bond silicon volumes.

Cooled silicon substrates for multilayer optics can also be manufactured with internal MC [41,54,55]. It was shown that the effect of the coating on temperature and deformation is insignificant. The thermal stress in multilayer optics depends on the difference in the coefficient of thermal expansion $k$ between the layer material and the substrate material, but does not depend on the difference $k$ between different sublayers. In principle, in order to minimize thermal stress, the coating material should have $k$ closer to $k$ substrates and/or a smaller Young modulus [55].

### 3.4. Indirect cooling methods for crystal monochromators

The development of optical elements with indirect cooling usually begins with an assessment of their effectiveness using FEM [30,35,39,56]. The cooling efficiency depends not only on the heat transfer coefficient, but also on the contact thermal resistance at the boundary between the crystal and the cooling unit. The thermal boundary resistance per unit contact area is defined as the ratio of the temperature jump at the interface to the thermal power per unit area flowing across the interface. Thermal resistance is mainly the result of phonon scattering at the interface due to the acoustic mismatch between dissimilar materials [57].

The key parameters influencing this thermal contact resistance are the applied pressure (contact pressure) and the state of the surface of the contact bodies at the interface [56]. Optimal conditions for thermal contact resistance in vacuum at ambient temperature were obtained in [57,58].

For two mating surfaces, even visually very smooth and flat, the actual contact area is usually less than 10% of the total area. It is in these areas that heat is transferred from one body to another. Therefore, due to the heat transfer paths, the heat flow in bodies near the interface is heterogeneous. In foil [59,60] or eutectic In-Ga [24,59,61–63] is often placed at the boundary between the crystal and the cooled block for obtaining a good thermal contact.

#### 3.4.1. Water cooling

The literature contains descriptions of water-cooled silicon [24,62,64] (Fig. 9), germanium [65], diamond monochromators [66,67], from the sides of the diamond monochromator [68], as well as from three sides of silicon monochromators [24] (Fig. 9).

#### 3.4.2. Cryogenic cooling

The design of a cryogenically cooled monochromator [69] is usually a simple rectangular silicon block sandwiched between two copper heat exchangers [34,56,60,70,71] (Fig. 10).

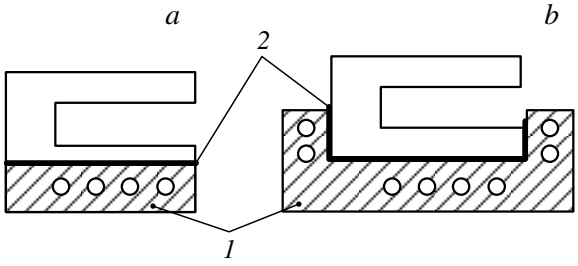


**Figure 9.** Cooling scheme of the back surface of the first arm of a two-crystal monoblock monochromator (*a*) and its three-sided cooling (*b*); *1* —copper substrate with channels for water circulation, *2* — eutectic layer In-Ga [24].

The clamping pressure of 5−10 bar is sufficient to obtain good thermal contact (see [57,58]) and does not cause significant deformation of the diffracting planes.

Two different methods are used at the boundary between silicon and copper to obtain good thermal contact: in some monochromators, an indium foil 0.5 mm thick is inserted between copper and silicon, and this foil can be coated with eutectic indium. In this case, the copper cooling units should be nickel-plated so that In-Ga does not diffuse into the copper. This foil improves thermal contact and, due to its relatively large thickness, limits the resulting stresses and strains transmitted to silicon at low temperatures. The surfaces of copper and silicon are finely polished to optical quality on other monochromators. For example, the size of the Si crystal was 50 mm wide, 90 mm long and 35 mm thick in the monochromator module described by the authors of [72]. Indium sheets were inserted between the crystal and the blocks for achieving good thermal contact. The blocks were pressed against the crystal by knife springs, providing pressure applied to the first crystal, 0.45 MPa.

The design of an indirect cryogenic cooling unit for a silicon crystal is described in [56] (Fig. 10, *a*): the crystal is located between two copper heat exchangers pressed against it at a pressure of about 0.4 MPa. Liquid nitrogen flows through 16 rectangular channels inside the cooling unit with a surface area of about 345 $cm^2$. The crystal dimensions are $60 \times 24 \times 40$ mm. Small and densely spaced cooling channels can significantly increase the heat exchange area, but at the same time the flow resistance increases. Therefore, the correct choice of channel structure is important for the efficiency of heat transfer, as well as for the stability of the cooling system (typical channel sizes: thickness 1 mm, height 8 mm [73]). Since the thermal conductivity of a silicon crystal is very high at 80 K (i.e., twice as high as that of copper), and the heat transfer coefficient of liquid nitrogen is quite small, large surface areas are required for heat transfer. Therefore, both the length and height of the cooling units are usually larger than that of the crystal. The result of the FEM simulation showed that such a design contributes to the removal of heat from the crystal surface [22].

Mechanical vibration is a critical problem for cryogenically cooled monochromators. It worsens the signal-to-noise ratio and the effective coherence of the radar beam. The usual sources of vibrations are sharp bends in the coolant lines and wavy inner surfaces of flexible tubes, which are difficult to avoid in practice. Vibrations can be minimized by rigid fastening of the monochromator, minimizing the flow rate, using flexible and, if possible, short hoses properly connected to the monochromator [60,72].

### 3.5. Direct or indirect cooling methods?

Each approach to the design of optical element cooling has its advantages and disadvantages [59]. The direct cooling mode can show better results than the side cooling mode. However, a comparison of some critical factors

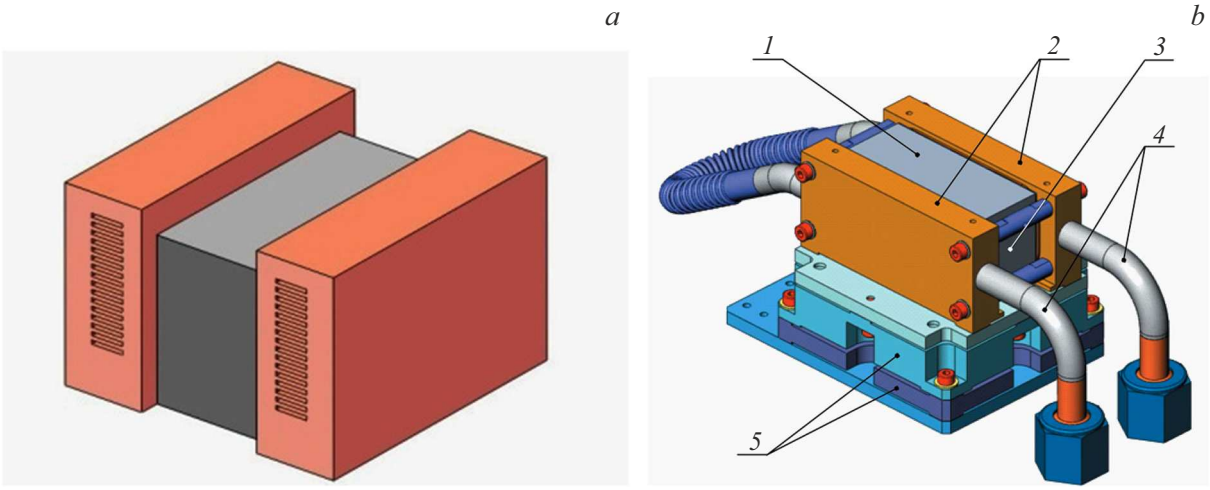


**Figure 10.** *a* — image of a crystal and its cooling blocks [56]; *b* — example of an assembly of a cooled monochromator. *1* — silicon crystal; *2* — copper heat exchangers; *3* — Pt 100 temperature sensor; *4* — stainless steel pipes; *5* — ceramic thermal insulation plates [71].

such as commercial cost, complexity of the production process, manufacturing period and problems with micro-vibration proved that the side cooling mode showed better technological performance [74,75]. Indeed, an indirect cooling system has a number of advantages. Firstly, the manufacturing of crystals with direct cooling is much more difficult, it is more time-consuming and expensive. Cutting coolant channels in silicon is a relatively slow process. On the other hand, contact-cooled crystals are usually simple rectangular blocks of single crystals of silicon. Secondly, crystals with direct cooling require vacuum sealing of the silicon-metal collector connection [48,76]. In[22], the seals were made of indium foil and metal sealing O-rings of C-shaped cross section. However, cyclic temperature changes can lead to loss of seal integrity. In addition, the sealing installation process itself is unreliable: it usually takes several attempts before a good vacuum seal is achieved. An indirect cooling crystal solves the problem of vacuum sealing, because only metal-to-metal seals are required, which are easy to perform.

### 3.6. Thin crystal

There is an approach based on the use of a very thin crystal. In this case, the thermal load can be limited by allowing most of the power of the SR beam not to be absorbed by the crystal. The crystal should be very thin for use at low energies and should not be exposed to deformation. The disadvantage of this method is the manufacturing and engineering problems that can be encountered in the manufacture and cooling of such a thin crystal [77].

A cryogenically cooled monochromator design using a thin crystal strategy is described in [78,79], which is capable of operating on SR sources at electron currents in the storage up to 300 mA. The key to the proposed design is the processing of a silicon crystal monoblock, which leaves a thin silicon plate with a thickness of about 0.6 mm enclosed between two identical blocks with indirect cooling (Fig. 11). Since the absorption coefficient of silicon becomes very small at high X-rays energies, a sufficiently thin crystal will absorb only part of the power of the incident SR beam. Another important factor is that the thermal conductivity of silicon at liquid nitrogen temperatures is so high that silicon can be cooled by surfaces at some reasonable distance from the thin part of the crystal. Cooling channels were drilled in both blocks, allowing liquid nitrogen to flow across the beam. A special C-ring forms a seal between a group of seven cooling channels and the coolant distribution manifold [78,79].

### 3.7. Inclined geometry of monochromator cooling

The expansion of the area of illumination of the surface of optical elements by an X-ray beam is the most effective way to further reduce thermal distortion of optical elements after selection of one of the possible cooling systems.

The geometry of skew-symmetric diffraction was used by Hounsari [80] and named „oblique“ (Fig. 12). The same geometry was proposed by Hrdi [81]. The angles of incidence of primary and reflected X-rays are equal in oblique geometry and the angle between the surface normal and the diffraction plane is $\beta$ (for symmetric and asymmetric diffraction $\beta = 0$). This means that only part of the thermal distortion will lie in the diffraction plane. Therefore, it can be expected that only a part of any deformation resulting from a high thermal load should contribute to the broadening of the rocking curve [82].

In the case of oblique geometry, the area of the beam trace on the crystal surface is defined as $A/\cos\beta \sin\theta_B$, where $A$ — the cross-sectional area of the primary beam.

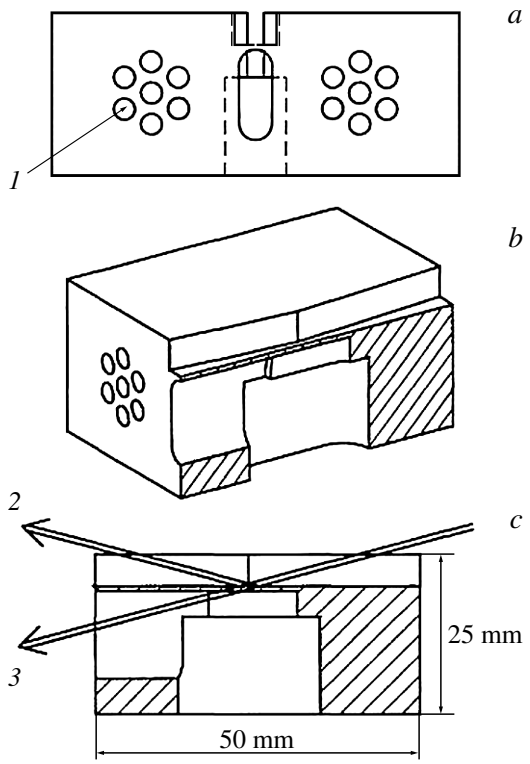


**Figure 11.** Cooling scheme of a thin silicon crystal: *a* — end view, *b* — general view of the half of the monoblock, *c* — cross section (*1* — cryogenic cooling channels, *2* — diffracted X-ray beam, *3* — passed X-ray beam) [77].

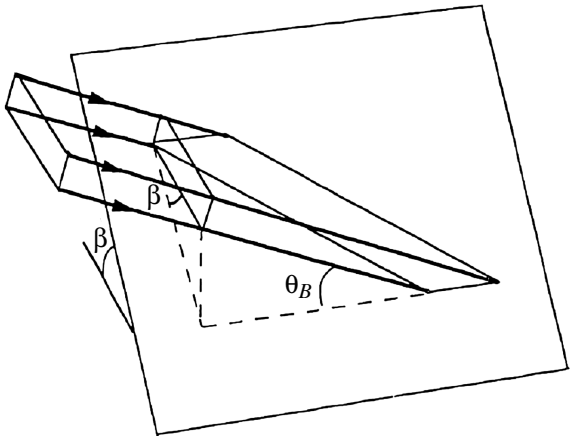


**Figure 12.** Scheme of formation of a trace of a radar beam in an oblique geometry on the crystal surface ($\beta$ — angle between the normal to the crystal surface and the diffraction plane, $\theta_B$ — Bragg angle) [79].

Consequently, the oblique geometry, compared with symmetric diffraction, gives a gain in the area of illumination by a factor of $1/\cos\beta$.

The area of the beam trace can also be increased by using asymmetric diffraction [83]. However, it should be noted that the use of asymmetric monochromators entails a decrease of the range of X-ray energy tuning and an increase of the photon flux [8].

A more detailed description of the oblique geometry can be found in [48,61,84–86].

### 3.8. Mirror cooling methods

Filters and apertures are used for reduction of the power of the SR beam, if possible, before the beam reaches the first optical element. In most cases, this optical element is a monochromator with a high thermal load, usually made of monocrystalline silicon. The absorbed power and heat flow can be significant, and the monochromator often has to be cryogenically cooled. The use of a grazing incidence mirror as the first optical element is an alternative approach to designing of a modern testing station [87]. However, this approach has drawbacks: it entails the design, manufacture and installation of cooled mirrors, which are usually large in size, require a long manufacturing time and can be expensive.

But it also has advantages [87]. Although the thermal power absorbed by the first mirror may be high, the absorbed heat flux is small, because unlike crystal monochromators, X-ray mirrors intercept the beam at small sliding angles. This fact greatly simplifies the thermal control of mirrors as the first optical elements. In addition, the use of a mirror approach reduces the thermal load on the components located behind the mirror, makes it possible to suppress harmonics and focus the beam, allows choosing the cut-off energy by using different strips of coating materials or sliding angles. Thus, if it is possible to develop simple, reliable and cost-effective mirrors, their advantages may outweigh their disadvantages. Using a mirror as the first optical element allows placing a conventional water-cooled silicon monochromator after it, which is much easier to manufacture, assemble, maintain and operate than its cryogenically cooled counterpart [59].

Water cooling is preferred option for most mirrors used on SR sources as the first optical element [88].

Silicon mirrors cooled with liquid nitrogen are much rarer, but still exist [89,90].

Thermal deformation can be decomposed into bending deformation caused by a temperature gradient along the depth of the mirror, and into „thermal mapping“ deformation [91] created by a temperature gradient because of uneven heat flow along the length of the mirror. Distortions of the „thermal mapping“ can be minimized by saturating the entire length of the mirror with an incident beam. When the power profile of the X-ray beam over the entire length of the optics is relatively uniform — a condition that can be fulfilled in many cases, for example, when using a cooling length less than the length of the beam trace [61.92] (Fig. 13, *a*) — the bending of the substrate remains the main component of distortion.

It is possible to imagine a mirror consisting of three segments, in which the central segment is heated by a beam, and the other two segments are cooled at its reflective

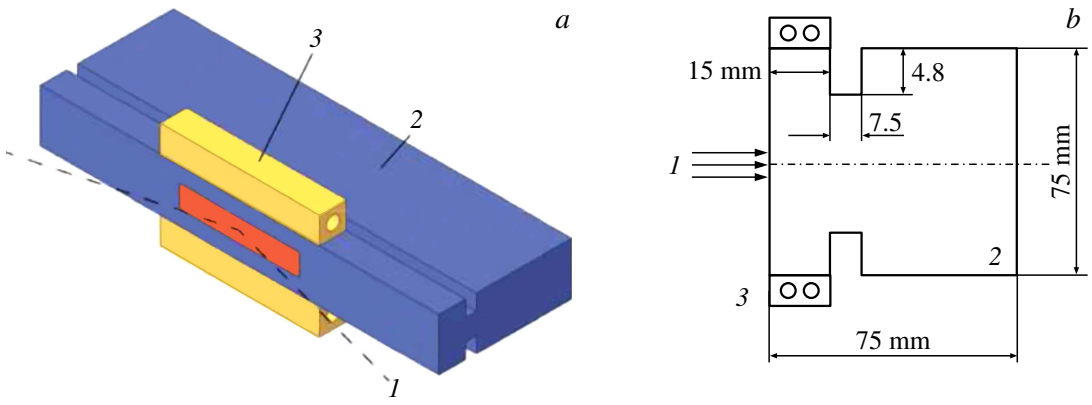


**Figure 13.** *a* — side-cooled water-cooled mirror design with „smart cutouts“ [89]; *b* — cross-section of the mirror with cutouts [91] (*1* — a beam of SR, *2* — mirror, *3* — water cooling channels).

surface. The central part deforms into a convex shape, and the other two segments, colder at the reflecting surface relative to the back, become concave. It is possible to obtain a thermomechanically balanced mirror without bending in case of proper designing. Cooling the reflective surface essentially creates a thermal moment opposite to that created by the central segment of the substrate. The authors of [59] called this scheme and the variations based on it, restoring the desired symmetry of the system, as the method of reverse thermal moment. It was found by [63,88,92] that the cooling units should be located close to the reflecting surface for providing the necessary reverse thermal torque. As expected, the location and width of the cooling units are critical parameters in this design, since they determine the magnitude of the reverse thermal moment applied to the mirror.

Studies showed that small „smart“ cutouts along the cooled sides of the mirror (Fig. 13, *b*) can increase the reverse bending moment [4,88,92,93].

Mirror cooling using a metal bath with In-Ga eutectic is widely used on SR sources as a heat transfer mechanism and a floating support without applying a load from the cooling unit to the mirror and eliminating the impact of gravity [76,93,94].

Heat transfer from the mirror *1* (Fig. 14, *a*) can be carried out through a thin layer In *3* to the cooled units *2*, then through In-Ga eutectic into the bath *4* and finally, into the coolant, which circulates through the cooling channels built into the bath [94]. Another method of heat transfer is the heat transfer through eutectic *3* (Fig. 14, *b*) and water-cooled copper plates *4* inserted into two grooves on the sides of the mirror *1* [76].

Indalloy 51 can also be used for heat transfer. This water-insoluble alloy is a metal with a mass percentage composition of Ga:In:Sn = 62.5:21.5:16, density 6.5g/cm$^3$, melting point 10.7°C and with thermal conductivity equivalent to stainless steel [95].

### 3.9. Adaptive cooling

The use of an adaptive X-ray mirror makes it possible to solve several tasks simultaneously, namely, to compensate for thermal deformation and variable curvature for focusing applications. Due to its inherent flexibility, adaptive optics can have useful and interesting applications in X-ray equipment, which makes this method very attractive [96].

From the rotating magnet of the storage ring, the SR propagates in the form of a wide fan of rays, which are collected by the first optical element of the experimental station. It is useful to increase the length of the mirror for maximizing the flow, and optical design may require that the optical surface of the mirror be longer than 1m.

The use of very long mirrors exposed to high thermal loads poses a serious challenge for the mechanical design of an effective cooling circuit. The variable beam trace, significantly smaller than the length of the mirror, causes a temperature change in the tangential direction.

#### 3.9.1. Temperature actuators

The real cooling system was developed and tested based on the idea described in the works [63,97]. Several cooling lengths were used for the variable length of the beam trace, when the photon energy changes, as well as several hydraulic valves to turn on/off the water flow.

The simplified solution used five cooling circuits [97] (Fig. 15). The mirror was cooled only on one side. It has a trough with Ga-In eutectic located 5 mm from the surface. A notch 20 mm from the surface is used to reduce heat shock and hold the mirror.

It may not be so convenient to have multiple cooling units and multiple hydraulic valves in some cases. Therefore, the authors of [63] proposed another adaptive method based on the principle of the use of one long cooling unit on each side of the mirror with additional electric heaters between the cooling units and the mirror, which reduced temperature gradients causing the distortion of

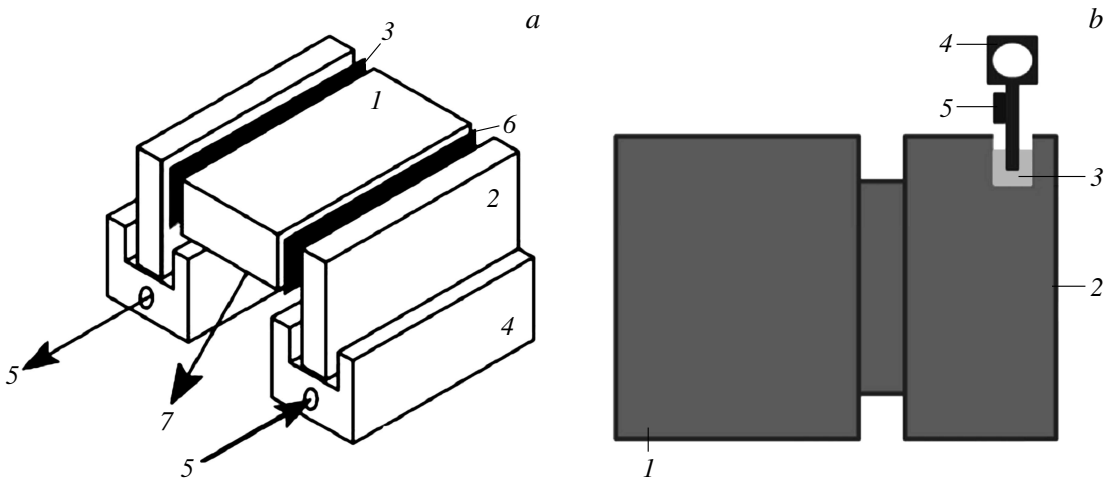


**Figure 14.** Mirror cooling schemes using a bath with In-Ga. *a*: *1* —mirror, *2* —cooling units, *3* — interlayer In, *4* — bath with In-Ga eutectic, *5* — direction of water circulation, *6* — SR beam, *7* — X-ray reflected from the lower surface of the mirror [93]; *b*: *1* — mirror, *2* —SR beam, *3* — In-Ga eutectic, *4* — water cooled copper plate, *5* — electric heater [94].

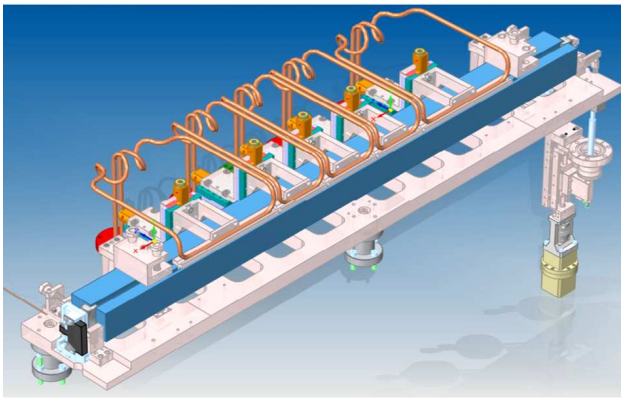

**Figure 15.** Real cooling system: mirror on its holder with five cooling circuits [97].

the mirror shape. The electric heaters consisted of a series of cells located along the entire length of the mirror. The method was called REAL (resistive element with adjustable length) subsequently [76]. Copper ribs (or blades) inserted into grooves filled with gallium-indium eutectic laid on the sides of the mirror were used for cooling. Resistive heaters were connected to the front of each blade at a safe distance from the eutectic (Fig. 14, *b*).

### 3.9.2. Piezoelectric actuators

A piezoelectric actuator (piezoactuator) is a device using piezoceramic's ability to expand under the action of the electrostatic field to generate force and movement in the micrometer range [98]. Piezoelectric actuators are used in microelectromechanical systems (MEMS), microrobots, bioengineering and medicine, as well as in the fields of vibration and noise control owing to the advantages of simple design, light weight and quick response.

The design of an adaptive mirror was described in [99]. The mirror was made of silicon carbide and cooled with water along its entire length, as shown in Fig. 16. The shape of its surface can be adjusted at two levels. The first level is mainly used to obtain the first rough shape and for focusing, and the second level is used for precise settings and correction of the temperature angle of inclination. The actuators can be piezoelectric or magnetostrictive.

The casing of the adaptive mirror described in [100] was made of graphite and coated with 0.1mm thick silicon carbide. These two materials provide a good trade off between thermomechanical properties and surface quality. The mirror itself consisted of three segments, because segmentation allows building very long mirrors. The central segment had a length of 50 cm, the extreme segments had a length of 25 cm. The width and thickness of the mirror were 10 and 3 cm, respectively. Each segment was independently controlled by a set of piezoelectric actuators: two rows each comprising three actuators for both end segments and two rows each comprising five actuators for the central segment. The use of two rows of actuators allows for adjusting the slope between

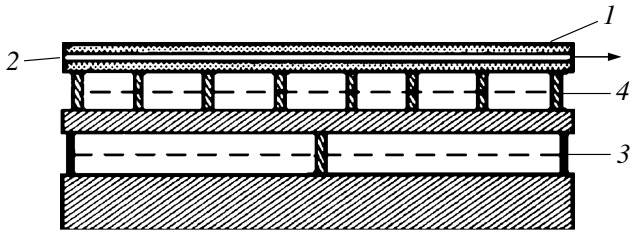


**Figure 16.** Diagram of a cooled adaptive X-ray mirror: *1* — reflective surface of the mirror, *2* — direction of water circulation, *3* — first level of correction, *4* — second level of correction [99].

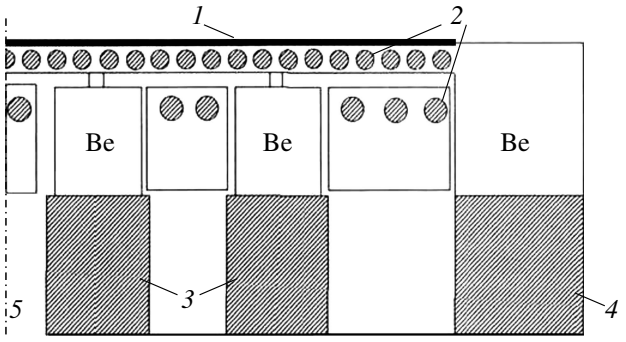


**Figure 17.** Adaptive cooled mirror diagram: *1* — thin plate of monocrystalline silicon, *2* — water cooling channels, *3* — point actuators, *4* — peripheral actuator, *5* — axis of symmetry [101].

the segments. The mirror was cooled by two water-cooled copper units located on both long sides of the mirror.

The peripheral actuator *4* (Fig. 17) and point actuators *3* attached to the back of the beryllium substrate described in [101] can change its shape and, consequently, the shape of the silicon crystal *1*. The wavefront was analyzed using a Shack-Hartmann sensor.

## 4. Methods for compensation of thermal stresses on FEL sources

Most of the FEL systems operate in the self-amplified spontaneous emission (SASE) mode nowadays [102]. FEL radiation comprises pulses with $\lambda \sim 0.05 - 0.16$ nm wavelength, $\sim 10 - 100$ fs duration and $\sim 1 - 3\,\mu$rad angular divergence [103]. The pulses are characterized by almost complete spatial coherence and very mediocre temporal coherence, resulting in a spectral pulse width of $\Delta E/E \sim 10^{-3}$ [104]. Self-seeding circuits [106,107] with a monochromator crystal between two segments of undulators were proposed for achieving a fully coherent FEL [105]. FEL SASE spectrum is filtered and a narrowband initial signal is generated when a monochromator is inserted into the undulator system. This signal then is amplified in subsequent segments of the undulator. Thus, the self-selection circuit dramatically improves the FEL spectral brightness.

An X-ray laser generator on free electrons is another light source for producing fully coherent pulses of hard X-ray radiation [108]. Its X-ray pulses circulate in an optical resonator formed by several reflecting crystals. The repetition rate of the electron bunch of a resonator of reasonable length should be about 1 MHz or higher. An intense X-ray pulses will create a high thermal load on crystal mirrors with an intracavity pulse energy of about $800\,\mu$J and a beam radius of about $50\,\mu$m at a repetition rate at the level of MHz [109].

The heat flux generated by FEL pulses can be several orders of magnitude higher compared with SR sources. For example, a typical FEL of Linac Coherent Light Source (LCLS) of the SLAC National Accelerator Laboratory, has a pulse energy of about 2 mJ, a transverse spot size of about $150\,\mu$m and a pulse duration of about 100 fs. The calculation of the average absorbed heat flux during the FEL pulse can provide the value $4 \cdot 10^{13}$ W/m$^2$. The existing cooling methods may not be sufficient to remove residual heat in the FEL area with such an extremely high heat flux.

A thin silicon single crystal is no longer effective under these conditions, because the 10 extinction lengths required for maximum Bragg reflectivity are comparable to the length of photoabsorption in silicon. On the contrary, 10 extinction lengths are approximately 1/10 of the photoabsorption length in diamond crystals. Precisely because the extinction length in diamond is much shorter than the absorption length, diamond crystals have close to 100% Bragg reflectivity even with backscattering and at the same time have high X-ray permeability [28]. However, it is difficult to manufacture such ultrathin crystalline components and handle them without causing any damage and deformation of the crystal. The solution is to use a monolithic crystal structure consisting of a thin membrane with a surrounding solid collar. This design allows for a mechanically stable installation of the membrane without deformations, while ensuring the effective heat dissipation [110]. Therefore, the authors of [111] produced a monolithic two-crystal monochromator, the first arm of which (P1) carried a thin membrane (Fig. 18). $5 \times 4 \times 4$ mm monochromator was cut from synthetically grown type IIa rough diamond.

The described diamond monoblock monochromator can be effectively used in self-selection systems with a relatively low pulse repetition rate. The low repetition rate below the damage threshold provides a relaxation time for the monochromator sufficient to dissipate the thermal energy released by the previous pulse and restore its original state before the arrival of the next FEL pulse. However, the monochromator does not have sufficient time for relaxation before the next FEL pulse in FEL systems with a high pulse repetition rate operating at the MHz frequency level [112].

The relaxation time can be described by the characteristic temperature spreading time due to heat transfer $\Delta_T$ [104,113]:

$$\Delta_T = r_1^2/4a^2 = r_1^2 c_p \rho/4\kappa, \qquad (5)$$

where $c_p$ — specific heat capacity, $\kappa$ — thermal conductivity, $\rho$ — crystal density, $r_1$ — transverse pulse size.

The heat capacity of diamond increases by almost 50 times with an increase of temperature from 100 to 600 K, and the thermal conductivity decreases by 7.6 times (Table. 3), but the heat transfer (cooling) time $\tau_T$ also increases sharply from 2 to $680\,\mu$s. The table shows that the operation at low temperatures is preferable for reducing the cooling time $\tau_T$, since the heat capacity in this case is small and the thermal conductivity is high [104].

The radiation in the European X-ray FEL comprises a series of pulses with a duration of $\approx 10 - 100$ fs. The pulses

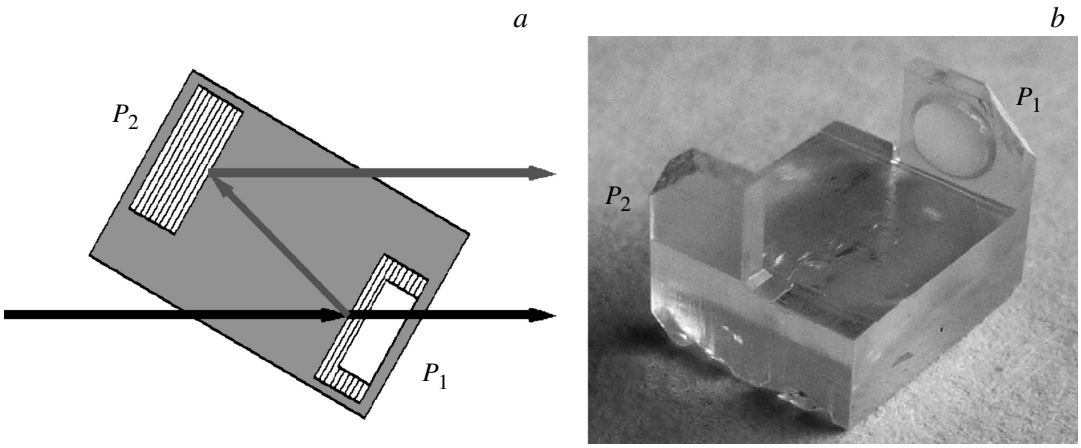


**Figure 18.** *a* — diagram of a monolithic double-crystal diamond monochromator with arms $P_1$ and $P_2$ for X-ray radiation 14.4 keV, reflex (800); *b* — photo of the monochromator after laser treatment and annealing in air at 630°C for 3 h [111].

**Table 3.** Coefficient of linear thermal expansion $\alpha_T \cdot 10^6$, specific heat $c_p$ ($J \cdot kg^{-1} \cdot K^{-1}$), thermal conductivity of diamond type I ($W \cdot m^{-1} \cdot K^{-1}$) [114] and characteristic cooling time $\tau_T$ depending on temperature $T$

| $T$, K | 100 | 200 | 300 | 400 | 600 |
|---|---|---|---|---|---|
| $\alpha_T$, $K^{-1}$ | 0.05 | 0.45 | 1.0 | 1.80 | 3.09 |
| $c_p$, | 29 | 214 | 514 | 854 | 1342 |
| $\kappa$ | 3050 | 1400 | 900 | 650 | 400 |
| $\tau_T$, $\mu$s | 1.9 | 31.0 | 115.8 | 266.4 | 680.2 |

Note. Wavelength 0.1 nm, reflection (400); pulse energy 557 $\mu$J, transverse pulse size $r_1 = 480\,\mu$m, density $\rho = 3.52\,g \cdot cm^{-3}$.

are grouped into packets with a duration of 0.6 ms and a repetition frequency of 10 Hz; the number of pulses in the packet is $\approx 2700$, and the time interval between them is $\Delta t_0 \approx 0.2\,\mu$s.

Unfortunately, the heat transfer times $\tau_T$ at $T_0 \geq 100$ K exceed the time intervals $\Delta t_0$ between pulses in a packet by 1–3 orders of magnitude. Therefore, the crystal temperature will increase during the exposure of the pulse packet to the crystal, and the heat will have time to dissipate only in the time intervals between the packets, since $\tau_T \ll 0.1$ s [104,113].

The authors of [115] studied the operation of a cryogenically cooled double-crystal monochromator Si(111) using SASE pulses arriving at a repetition rate of 2.25MHz. It was shown that the transmission of the monochromator decreases by about two times after $\sim 150$ pulses (which in this case corresponded to the total incident energy $\sim 50$ mJ).

Nevertheless, as the first monochromator, the diamond-based design with liquid nitrogen cooling seems to be the most promising. Silicon monochromators can be useful as secondary optical elements located closer to experimental stations.

Adaptive methods with variable length cooling and thermoregulation along its entire length are used to compensate for thermal stresses, similar to those described in Sect. 3.9 in case of usage of a mirror as the first optical element in the FEL beam channel [97,116,117].

Problems of designing a cooling system arise when a monochromator in self-selection mode is considered [3]. The monochromator can be a thin diamond plate [118]. It is necessary to implement a clamping mechanism to obtain a sufficient heat transfer area and tight contact for ensuring cooling of such a thin plate. Unfortunately, this clamping can cause severe deformation, which, in turn, can result in a degradation of the efficiency of self-selection. Cutouts in a thin diamond plate sacrificing the efficiency of heat transfer comprise one of the existing solutions (Fig. 19, *a*) [118].

A thick base is added to the lamellar diamond crystal in another monochromator design. The thick base acts as a cooler and also as a stress-free attachment point. The attachment of a thick base can significantly reduce thermal resistance. On the other hand, it also ensures strong resistance to the strains that occurs during clamping because of its large thickness. Moreover, the greater thickness also improves the effective thermal conductivity of the base and, therefore, the cooling capacity. The monochromator has a trapezoidal shape (Fig. 19, *b*). It is carefully inserted into the holder for installation and is sealed from the bottom to prevent the crystal from slipping out of the holder [119].

## Conclusion

It follows from the above that it is possible to successfully compensate for thermal distortions of optical elements created by SR sources by combining various crystals, coolants and cooling methods. The efficiency of such compensation can be increased by additional use of thin

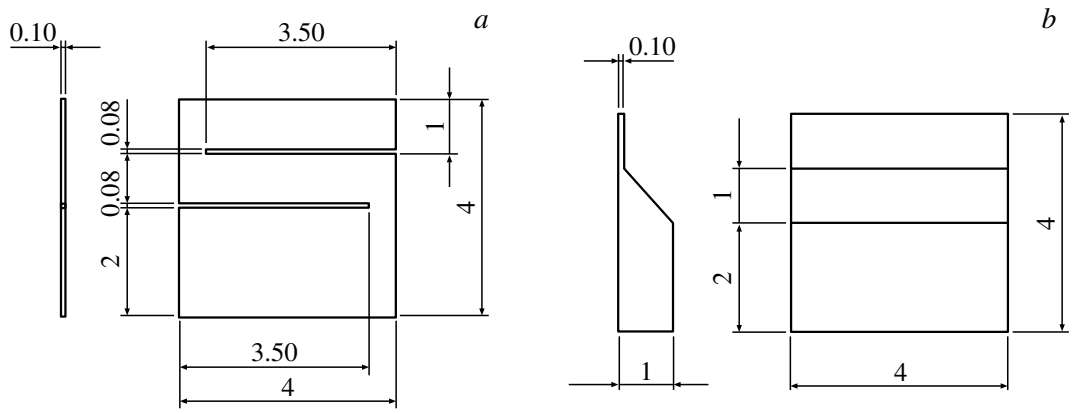


**Figure 19.** Two geometric designs of the diamond monochromator used in self-selection mode: *a* —the monochromator has two cutouts to relieve the stress created by the clamping part of the holder; *b* — the trapezoidal monochromator has a thick base with a thin tip [3].

crystal or inclined geometry methods, as well as by adaptive optics.

Moreover, apparently, it makes sense to use adaptive optics consisting of two elements in some cases: the second element is designed to correct the distortion of the wavefront created by the first element [120].

It was shown that the use of cryogenically cooled synthetic diamond crystal has a good potential for compensating the thermal stresses created by X-ray FEL. However, there is still a lot of work to be done to develop methods for controlling distortions of the crystal lattice introduced by a separate pulse packet, as well as relaxation of the lattice during the time separating the previous and subsequent pulses. It is necessary to develop methods for obtaining diamonds of high structural perfection and large size despite certain achievements in the growing of diamond synthetic single crystals [121].

### Funding

The study has been performed under the state assignment of National Research Center „Kurchatov Institute“.

### Conflict of interest

The author declares that he has no conflict of interest.

## References

[1] Y. Hwu, G. Margaritondo. J. Synchrotron Rad., **28** (3), 1014 (2021). DOI: 10.1107/S1600577521003325
[2] H.C.N. Tolentino, M.M. Soares, F.M.C. Silva, J.H. Rezende, D. Puglia, A. Bordin, M.S. Silva, R.R. Geraldes. AIP Conf. Proc., **2054** (1), 060026 (2019). DOI: 10.1063/1.5084657
[3] Z. Qu. *Photo-Thermo-Mechanical Analysis and Control for High-brightness and High-repetition-rate X-ray Optics* (Dis., Spring, 2020)
[4] E. Prat. arXiv:2107.09131v1. [physics.acc-ph] (2021). DOI: 10.48550/arXiv.2107.09131
[5] R.K. Smither. Nucl. Instrum. Meth. A, **291** (1−2), 286 (1990). DOI: 10.1016/0168-9002(90)90075-H
[6] A. Khounsary, P. Strons, N. Kujala, A. Macrander. Proc. SPIE., **8502**, 85020C (2012). DOI: 10.1117/12.960243
[7] D.H. Bilderback, A.K. Freund, G.S. Knapp, D.M. Mills. J. Synchrotron Rad., **7** (2), 53 (2000). DOI: 10.1107/S0909049500000650.
[8] L. Assoufid, W.-K. Lee, D.M. Mills. Rev. Sci. Instrum., **66** (3), 2713 (1995). DOI: 10.1063/1.1145615
[9] V. Mocella, W.-K. Lee, G. Tajiri, D. Mills, C. Ferrero, Y. Epelboin. J. Appl. Cryst., **36** (1), 129 (2003). DOI: 10.1107/S0021889802020526
[10] L. Zhang, M. Sánchez del Río, G. Monaco, C. Detlefs, T. Roth, A.I. Chumakov, P. Glatzel. J. Synchrotron Rad., **20** (4), 567 (2013). DOI: 10.1107/S0909049513009436
[11] H. Khosroabadi, L. Alianelli, D.G. Porter, S. Collins, K. Sawhney. J. Synchrotron Rad., **29** (2), 377 (2022). DOI: 10.1107/S160057752200039X
[12] K.-Y. Kao, H.-S. Fung, H.-Y. Chao, S.-C. Yeh, J.-H. Chen. J. Phys. Conf. Series, **2380** (1), 012076 (2022). DOI: 10.1088/1742-6596/2380/1/012076
[13] H. Wang, S. Berujon, J. Sutter, S.G. Alcock, K. Sawhney. Proc. SPIE, **9206**, 920608 (2014). DOI: 10.1117/12.2062828
[14] O.Soloviev, G. Vdovin. Opt. Express, **13** (23), 9570 (2005). DOI: 10.1364/OPEX.13.009570
[15] Y. Kayser, C. David, U. Flechsig, J. Krempasky, V. Schlott, R. Abela. J. Synchrotron Rad., **24** (1), 150 (2017). DOI: 10.1107/S1600577516017562
[16] L. Xue, H. Luo, Q. Diao, F. Yang, J. Wang, Z. Li. Sensors, **20** (22), 6660 (2020). DOI: 10.3390/s20226660
[17] C.M. Kewish, P. Thibault, M. Dierolf, O. Bunk, A. Menzel, J. Vila-Comamala, K. Jefimovs, F. Pfeiffer. Ultramicroscopy, **110** (4), 325 (2010). DOI: 10.1016/j.ultramic.2010.01.004
[18] S. Rutishauser, A. Rack, T. Weitkamp, Y. Kayser, C. David, A.T. Macrander. J. Synchrotron Rad., **20** (2), 300 (2013). DOI: 10.1107/S0909049513001817
[19] P. Revesz, A. Kazimirov, I. Bazarov. Nucl. Instrum. Meth. A, **576** (2), 422 (2007). DOI: 10.1016/j.nima.2007.02.110
[20] P. Revesz, J.A. White. Nucl. Instrum. Meth. A, **540** (2), 470 (2005). DOI: 10.1016/j.nima.2004.11.04
[21] V.I. Subbotin, V.S. Kolesov, Yu.A. Kuz'Min, V.V. Kharitonov. Sov. Phys. Dokl., **33** (8), 633 (1988).

[22] W.-K. Lee, K. Fezzaa, P. Fernandez, G. Tajiri, D. Mills. J. Synchrotron Rad., **8** (1), 22 (2001). DOI: 10.1107/s0909049500013868
[23] V. Rehn. Proc. SPIE, **0582**, 238 (1986). DOI: 10.1117/12.950935
[24] D.H. Bilderback, D.M. Mills, B.W. Batterman, C. Henderson. Nucl. Instrum. Meth. A, **246** (1−3), 428 (1986). DOI: 10.1016/0168-9002(86)90125-7
[25] R.C. Burns, A.I. Chumakov, S.H. Connell, D. Dube, H.P. Godfried, J.O. Hansen, J. Härtwig, J. Hoszowska, F. Masiello, L. Mkhonza, M. Rebak, A. Rommevaux, R. Setshedi, P. Van Vaerenbergh. J. Phys. Cond. Matter., **21** (36), 364224 (2009). DOI: 10.1088/0953-8984/21/36/364224
[26] A.V. Inyushkin, A.N. Taldenkov, V.G. Ralchenko, A.P. Bolshakov, A.V. Koliadin, A.N. Katrusha. Phys. Rev. B, **97** (14), 144305 (2018). DOI: 10.1103/PhysRevB.97.144305
[27] S. Stoupin, Yu.V. Shvyd'ko. Phys. Rev. B, **83** (10), 104102 (2011). DOI: 10.1103/PhysRevB.83.104102
[28] Yu.V. Shvyd'ko, S. Stoupin, V. Blank, S. Terentyev. Nature Photon., **5** (9), 539 (2011). DOI: 10.1038/nphoton.2011.197
[29] A.K. Freund. Opt. Eng., **34** (2), 432 (1995). DOI: 10.1117/12.195195
[30] L. Zhang, W.-K. Lee, M. Wulff, L. Eybert. J. Synchrotron Rad., **10** (4), 313 (2003). DOI: 10.1107/S0909049503012135
[31] J. Härtwig, S. Connell. Synchrotron Radiation News, **18** (1), 15 (2005). DOI: 10.1080/08940880500457487
[32] R.K. Smither. Proc. SPIE, **1739**, 116 (1993).
[33] L. Assoufid, K.W. Quast, H.L.T. Nian. Proc. SPIE, **2855**, 250 (1996). DOI: 10.1117/12.259836
[34] L. Zhang. Proc. SPIE, **1997**, 223 (1993). DOI: 10.1117/12.163803
[35] R. Huang, D.H. Bilderback, K. Finkelstein. J. Synchrotron Rad., **21** (2), 366 (2014). DOI: 10.1107/S1600577514000514
[36] R. Cernik, M. Hart. Nucl. Instrum. Meth. A, **281** (2), 403 (1989). DOI: 10.1016/0168-9002(89)91342-9
[37] L.E. Berman, M. Hart. Rev. Sci. Instrum., **63** (1), 437 (1992). DOI: 10.1063/1.1142723
[38] M.R. Howells. Opt. Eng., **35** (4), 1187 (1996). DOI: 10.1117/1.600607
[39] I.P. Dolbnya, K.J.S. Sawhney, S.M. Scott, A.J. Dent, G. Cibin, G.M. Preece, U.K. Pedersen, J. Kellya, P. Murray. J. Synchrotron Rad., **26** (1), 253 (2019). DOI: 10.1107/S1600577518014662
[40] J. Arthur, W.H. Tompkins, C. Troxel Jr, R.J. Contolini, E. Schmitt, D.H. Bilderback, C. Henderson, J. White, T. Settersten. Rev. Sci. Instrum., **63** (1), 433 (1992). DOI: 10.1063/1.1142722
[41] R.L. Headrick, K.W. Smolenski, A. Kazimirov. Rev. Sci. Instrum., **73** (3), 1476 (2002). DOI: 10.1063/1.1435819
[42] H. Yamazaki, Y. Shimizu, H. Kimura, S. Watanabe, Hi. Ono, T. Ishikawa. AIP Conf. Proc., **879** (1), 946 (2007). DOI: 10.1063/1.2436218.
[43] J.R. Arthur. Opt. Eng., **34** (2), 441 (1995). DOI: 10.1117/12.195395
[44] K.W. Smolenski, Q. Shen, P. Doing. AIP Conf. Proc, **417** (1), 66 (1997). DOI: 10.1063/1.54628
[45] A.K. Freund, J.R. Arthur, L. Zhang. Proc. SPIE, **3151**, 216 (1997). DOI: 10.1117/12.294481
[46] P. Oberta, V. Áč, J. Hrdy, B. Lukás. J. Synchrotron Rad., **15** (6), 543 (2008). DOI: 10.1107/S0909049508027374
[47] A. Artemev, N. Artemiev, E. Busetto, J. Hrdy, D. Mrazek, I. Plešek, A. Savoia. Nucl. Instrum. Meth A, **467** (1), 380 (2001). DOI: 10.1016/S0168-9002(01)00330-8
[48] W.K. Lee, A.T. Macrander, D.M. Mills, C.S. Rogers, R.K. Smither, A.M. Khounsary. Nucl. Instrum. Meth. A, **320** (1−2), 381 (1992). DOI: 10.1016/0168-9002(92)90798-9
[49] L. Assoufid, K.W. Quast, H.L.T. Nian Proc. SPIE, **2855**, 250 (1996). DOI: 10.1117/12.259836
[50] W.-K. Lee, P. Fernandez, D.M. Mills. J. Synchrotron Rad., **7** (1), 12 (2000). DOI: 10.1107/S0909049599014478
[51] N.G. Kujala, A.T. Macrander, M. Ramanathan, E.M. Dufresne, G. Navrotski, S. Marathe, L. Assoufid, D.M. Mills, D.C. Mancini. J. Phys. Conf. Series, **425** (5), 052006 (2013). DOI: 10.1088/1742-6596/425/5/052006
[52] M. Kuroda, H. Yamaoka, T. Ishikawa. SPring-8 Annual Report, **1**, 205 (1994).
[53] H. Yamazaki, Y. Shimizu, N. Shimizu, M. Kawamoto, Y. Kawano, Y. Senba, H. Ohashi, S. Goto. Proc. SPIE, **7077**, 707719 (2008). DOI: 10.1117/12.796685
[54] A. Kazimirov, D.-M. Smilgies, Q. Shen, X. Xiao, Q. Hao, E. Fontes, D.H. Bilderback, S.M. Gruner, Y. Platonov, V.V. Martynov. J. Synchrotron Rad., **13** (2), 204 (2006). DOI: 10.1107/S0909049506002846
[55] X. Cheng, L. Zhang, C. Morawe, M. Sánchez del Río. J. Synchrotron Rad., **22** (2), 317 (2015). DOI: 10.1107/s1600577514026009
[56] H. Wang. AIP Adv., **9** (8), 085007 (2019). DOI: 10.1063/1.5109807
[57] E. Gmelin, M. Asen-Palmer, M. Reuther, R. Villar. J. Phys. D: Appl. Phys., **32** (6), R19 (1999). DOI: 10.1088/0022-3727/32/6/004
[58] A.M. Khounsary, D. Chojnowski, L. Assoufid, W.M. Worek. Proc. SPIE, **3151**, 45 (1997). DOI: 10.1117/12.294497
[59] A.M. Khounsary, W. Yun, I. McNulty, Z. Cai, B.P. Lai. Proc. SPIE, **3447**, 81 (1998). DOI: 10.1117/12.331120
[60] A. Chumakov, R. Rüffer, O. Leupold, J.P. Celse, K. Martel, M. Rossata, W.-K. Lee. J. Synchrotron Rad., **11** (2), 132 (2004). DOI: 10.1107/S0909049503026785
[61] Z. Xu, N. Wang. J. Synchrotron Rad., **19** (3), 428 (2012). DOI: 10.1107/S0909049512004050
[62] H. Kawata, M. Sato, Y. Higashi, H. Yamaoka. J. Synchrotron Rad., **5** (3), 673 (1998). DOI: 10.1107/S0909049597020268
[63] L. Zhang, D. Cocco, N. Kelez, D.S. Morton, V. Srinivasana, P.M. Stefan. J. Synchrotron Rad., **22** (5), 1170 (2015). DOI: 10.1107/S1600577515013090
[64] H. Yamaoka, N. Hiraoka, M. Ito, M. Mizumaki, Y. Sakurai, Y. Kakutani, A. Koizumi, N. Sakai, Y. Higashi. J. Synchrotron Rad., **7** (2), 69 (2000). DOI: 10.1107/S090904959901691X
[65] Y. Li, A. Khounsary, S. Narayanan, A. Macrander, R. Khachatryan, L. Lurio Proc. SPIE, **5537**, 189 (2004). DOI: 10.1117/12.564241
[66] P.B. Fernandez, T. Graber, S. Krasnicki, W.-K. Lee, D.M. Mills, C.S. Rogers, L. Assoufid. AIP Conf. Proc., **417** (1), 89 (1997). DOI: 10.1063/1.54594
[67] P. Van Vaerenbergh, C. Detlefs, J. Härtwig, T.A. Lafford, F. Masiello, T. Roth, W. Schmid, P. Wattecamps, L. Zhang. AIP Conf. Proc., **1234** (1), 229 (2010). DOI: 10.1063/1.3463179

[68] R.C. Blasdell, L.A. Assoufid, D.M. Mills. *Argonne National Laboratory Report* ANL/APS/TB-24 (US DOE) (1995)
[69] G. Marot. Opt. Eng., **34** (2), 426 (1995). DOI: 10.1117/12.195196
[70] A.V. Zozulya, A. Shabalin, H. Schulte-Schrepping, J. Heuer, M. Spiwek, I. Sergeev, I. Besedin, I.A. Vartanyants, M. Sprung. J. Phys. Conf. Series, **499** (1), 012003 (2014). DOI: 10.1088/1742-6596/499/1/012003
[71] A.I. Chumakov, I. Sergeev, J.-P. Celse, R. Rüffer, M. Lesourd, L. Zhang, M. Sánchez del Río. J. Synchrotron Rad., **21** (2), 315 (2014). DOI:10.1107/S1600577513033158
[72] T. Mochizuki, S. Goto, T. Ishikawa. Proc. MEDSI'04, 10 (2004).
[73] P. Marion, L. Zhang, L. Goirand, M. Rossat, K. Martel. Proc. MEDSI 2006 (Hyogo, Jpn, 2006)
[74] A. Khounsary. Proc. SPIE, **3773**, 78 (1999). DOI: 10.1117/12.370114.
[75] L.-M. Jin, W.-Q. Zhu, Y. Wang, N.-X. Wang, J.-F. Cao, Z.-M. Xu. Nucl. Instrum. Meth. A, **902** (6), 190 (2018). DOI: 10.1016/j.nima.2018.06.015
[76] D. Cocco, C. Hardin, D. Morton, L. Lee, M. Ling Ng, L. Zhang, L. Assoufid, W. Grizolli, X. Shi, D.A. Walko, G. Cutler, K.A. Goldberg, A. Wojdyla, M. Idir, L. Huang, G. Dovillaire. Opt. Express., **28** (13), 19242 (2020). DOI: 10.1364/OE.394310
[77] G.S. Knapp, M.A. Beno, C.S. Rogers, C.L. Wiley, P.L. Cowan. Rev. Sci. Instrum., **65** (9), 2792 (1994). DOI: 10.1063/1.1145222
[78] G.S. Knapp, C.S. Rogers, M.A. Beno, G. Jennings, P.L. Cowan. Rev. Sci. Instrum., **66** (2), 2138 (1995). DOI: 10.1063/1.1145752
[79] C.S. Rogers, D.M. Mills, W.K. Lee, G.S. Knapp, J. Holmberg, A.K. Freund, M. Wulif, M. Rossat, M. Hanfland, H. Yamaoka. Rev. Sci. Instr., **66** (6), 3494 (1995). DOI: 10.1063/1.1145460
[80] A.M. Khounsary. Rev. Sci. Instrum., **63** (1), 461 (1992). DOI: 10.1063/1.1142732
[81] J. Hrdy. Rev. Sci. Instrum., **63** (1), 459 (1992). DOI: 10.1063/1.1142731
[82] A.T. Macrander, W.K. Lee, R.K. Smither, D.M. Mills, C.S. Rogers, A.M. Khounsary. Nucl. Instrum. Meth. A, **319** (1−3), 188 (1992). DOI: 10.1016/0168-9002(92)90553-G
[83] R.K. Smither, P.B. Fernandez. Nucl. Instrum. Meth. A, **347** (1−3), 313 (1994). DOI: 10.1016/0168-9002(94)91900-3
[84] H. Yamazaki, M. Yabashi, K. Tamasaku, Y. Yoneda, S. Goto, T. Mochizuki, T. Ishikawa. Nucl. Instrum. Meth. A, **467−468** (1), 643 (2001). DOI: 10.1016/S0168-9002(01)00435-1
[85] P. Oberta, V. Áč, J. Hrdý. J. Synchrotron Rad., **15** (1), 8 (2008). DOI: 10.1107/S0909049507044858
[86] R.K. Smither, T.J. Graber, P.B. Fernandez, D.M. Mills. Rev. Sci. Instrum., **83** (3), 035107 (2012). DOI: 10.1063/1.3685614
[87] W. Yun, A. Khounsary, B. Lai, K.J. Randall, I. McNulty, E. Gluskin, D. Shu. Rev. Sci. Instrum., **67** (9), 3353 (1996). DOI: 10.1063/1.1147398
[88] L. Zhang, R. Barrett, K. Friedrich, P. Glatzel, T. Mairs, P. Marion, G. Monaco, C. Morawe, T. Weng. J. Phys. Conf. Series, **425** (5), 052029 (2013). DOI: 10.1088/1742-6596/425/5/052029
[89] G. Cutler, D. Cocco, E. DiMasi, S. Morton, M. Sanchez del Rio, H. Padmore. J. Synchrotron Rad., **27** (5), 1131 (2020). DOI: 10.1107/S1600577520008930
[90] A. Wojdyla, K.A. Goldberg. Synchrotron Rad. News, **34** (6), 1 (2022). DOI: 10.1080/08940886.2021.2022398
[91] P. Brumund, J. Reyes-Herrera, C. Morawe, T. Dufrane, H. Isern, T. Brochard, M. Sánchez del Río, C. Detlefs. J. Synchrotron Rad., **28** (5), 1423 (2021). DOI: 10.1107/S160057752100758X
[92] Y. Li, A. Khounsary, J. Maser, S. Nair. Proc. SPIE, **5193**, 204 (2004). DOI: 10.1107/S0909049512004050
[93] S. Wang, D. Zhang, M. Li, L. Gao, M. Chen, F. Yanga, W. Sheng. J. Synchrotron Rad., **29** (5), 1152 (2022). DOI: 10.1107/S1600577522007160
[94] H. Ohashi, Y. Tamenori, T. Mochizuki, T. Ishikawa. AIP Conf. Proc., **705** (1), 667 (2004). DOI: 10.1063/1.1757884
[95] M.R. Sullivan, S. Rekhi, J. Bohon, S. Gupta, D. Abel, J. Toomey, M.R. Chance Rev. Sci. Instrum., **79** (2), 025101 (2008). DOI: 10.1063/1.2839027
[96] J. Susini, G. Forstner, L. Zhang, C. Boyer, R. Ravelet. Rev. Sci. Instrum., **63** (1), 423 (1992). DOI: 10.1063/1.1142720
[97] C.L. Hardin, V.N. Srinivasan, L. Amores. N.M. Kelez, D.S. Morton, P.M. Stefan, J. Nicolas, L. Zhang, D. Cocco. Proc. SPIE, **9965**, 996505 (2016). DOI: 10.1117/12.223582
[98] H. Liu, J. Zhong, C. Lee, S.-W. Lee, L. Lin. Appl. Phys. Rev., **5** (4), 041306 (2018). DOI: 10.1063/1.5074184
[99] A.K. Freund, F. de Bergevin, G. Marot, C. Riekel, J. Susini, L. Zhang, E. Ziegler. Opt. Eng., **29** (8), 928 (1990). DOI: 10.1117/12.55678
[100] J. Susini, G. Marot, L. Zhang, R. Ravelet, P. Jagourel. Rev. Sci. Instrum., **63** (1), 489 (1992). DOI: 10.1063/1.1142740
[101] D. Dézoret, R. Marmoret, A. Freund, Å. Kvick, R. Ravelet. J. de Physique IV Proc., **04** (C9), 41 (1994). DOI: 10.1051/jp4:1994906
[102] R. Bonifacio, C. Pellegrini, L.M. Narducci. Opt. Commun., **50** (6), 373 (1984). DOI: 10.1016/0030-4018(84)90105-6
[103] G. Geloni, E. Saldin, L. Samoylova, E. Schneidmiller, H. Sinn, Th. Tschentscher, M. Yurkov. New J. Phys., **12** (3), 035021 (2010). DOI: 10.1088/1367-2630/12/3/035021
[104] V. Bushuev. Bull. Russ. Acad. Sci.: Phys., **77** (1), 15 (2013).
[105] C. Feng, H.-X. Deng. Nucl. Sci. Tech., **29** (11), 160 (2018). DOI: 10.1007/s41365-018-0490-1
[106] G. Geloni, V. Kocharyan, E. Saldin. J. Mod. Opt., **58** (16), 1391 (2011). DOI: 10.1080/09500340.2011.586473
[107] I. Inoue, T. Osaka, T. Hara, T. Tanaka, T. Inagaki, T. Fukui, S. Goto, Y. Inubushi, H. Kimura, R. Kinjo, H. Ohashi, K. Togawa, K. Tono, M. Yamaga, H. Tanaka, T. Ishikawa, M. Yabashi. Nature Photon., **13** (5), 319 (2019). DOI: 10.1038/s41566-019-0365-y
[108] R.R. Lindberg, K.J. Kim, Y. Shvyd'ko, W.M. Fawley. Phys. Rev. Accel. Beams, **14** (1), 010701 (2011). DOI: 10.1103/PhysRevSTAB.14.010701
[109] N. Huang, H. Deng. Phys. Rev. Accel. Beams, **23** (9), 090704 (2020). DOI: 10.1103/PhysRevAccelBeams.23.090704
[110] T. Kolodziej, P. Vodnala, S. Terentyev, V. Blank, Yu. Shvyd'ko. J. Appl. Cryst., **49** (4), 1240 (2016). DOI: 10.1107/S1600576716009171
[111] Y. Shvyd'ko, S. Terentyev, V. Blank, T. Kolodziej. J. Synchrotron Rad., **28** (6), 1720 (2021). DOI: 10.1107/S1600577521007943

[112] B. Yang, S. Wang, J. Wu. J. Synchrotron Rad., **25** (1), 166 (2018). DOI: 10.1107/S1600577517015466
[113] V. Bushuev. J. Surf. Invest.: X-Ray, Synchrotron Neutron Tech., **10** (6), 1179 (2016).
[114] I.S. Grigoryev, E.Z. Mejlikhov (red.). *Fizicheskie velichiny: Spravochnik.* (Energoatomizdat, M., 1991) (in Russian).
[115] I. Petrov, U. Boesenberg, V. A. Bushuev, J. Hallmann, K. Kazarian, W. Lu, J. Müller, M. Reiser, A. Rodriguez-Fernandez, L. Samoylova, M. Scholz, H. Sinn, A. Zozulya, A. Madsen. Opt. Express., **30** (4), 4978 (2022). DOI: 10.1364/OE.451110
[116] F. Yang, H. Sinn, A. Trapp, R. Signorato, T. Noll. Proc. MEDSI 2012 (Shanghai, China. SINAP, 2012), p.6.
[117] R.J. Bean, A. Aquila, L. Samoylova, A.P. Mancuso. J. Opt., **18** (7), 074011 (2016). DOI: 10.1088/2040-8978/18/7/074011
[118] L. Samoylova, D. Shu, X. Dong, G. Geloni, S. Karabekyan, S. Terentev, V. Blank, S. Liu, T. Wohlenberg, W. Decking, H. Sinn. AIP Conf. Proc., **2054** (1), 030016 (2019). DOI: 10.1063/1.5084579
[119] D. Shu, Y. Shvyd'ko, J. Amann, P. Emma, S. Stoupin, J. Quintana. J. Phys. Conf. Series, **425** (5), 052004 (2013). DOI: 10.1088/1742-6596/425/5/052004
[120] M. Sanchez del Rio, A. Wojdyla, K.A. Goldberg, G.D. Cutler, D. Cocco, H.A. Padmore. J. Synchrotron Rad., **27** (5), 1141 (2020). DOI: 10.1107/S1600577520009522
[121] S. Stoupin, S. Antipov, J.E. Butler, A.V. Kolyadin, A. Katrusha. J. Synchrotron Rad., **23** (5), 1118 (2016). DOI: 10.1107/S1600577516011796

*Translated by A.Akhtyamov*